Supplementary Information

Asymmetric electronic modulation in bridged Cu-O-Ni dual-atom catalysts promoting CO_2 electroreduction

Xue Bai [a], Liyuan Xiao [a], Xiaoqin Xu [a], Anaer Husile [a], Fuquan Bai [b], Lina Li [c*] and Jingqi Guan [a*]

[a] Institute of Physical Chemistry, National Demonstration Center for Experimental Chemistry Education, College of Chemistry, Jilin University, Changchun 130021, China. *E-mail: guanjq@jlu.edu.cn (J.Q. Guan)

[b] Laboratory of Theoretical and Computational Chemistry, Institute of Theoretical Chemistry, College of Chemistry, Jilin University， Changchun, 130023 China.

[c] Shanghai Synchrotron Radiation Facility, Shanghai Advanced Research Institute, Shanghai, 201204. *E-mail: lilina@sinap.ac.cn (L.N. Li)

Chemicals

3-methoxysalicylaldehyde, ethylenediamine, methanol, $Cu(OAc)_2 \cdot H_2O$, ethanol, dimethylformamide, $Ni(NO_3)_2 \cdot 6H_2O$ and Et_2O were purchased from commercial suppliers and used as received.

Structure characterizations

High-resolution TEM (HRTEM) images were recorded on a JEM-2100 transmission electron microscope (Tokyo, Japan) at 200 kV. The valence state was determined using XPS recorded on a Thermo ESCALAB 250Xi. The X-ray source selected was monochromatized Al Kα source (15 kV, 10.8mA). Region scans were collected using 30-eV pass energy. Peak positions were calibrated relative to C 1s peak position at 284.6 eV.

X-ray absorption data collection

The X-ray absorption fine structure (XAFS) spectra were performed at BL11B beamline of Shanghai Synchrotron Radiation Facility (SSRF) operated at 3.5 GeV under "top-up" mode with a constant current of 240 mA. The XAFS data were recorded under fluorescence mode with a 7-element Ge solid state detector. The energy was calibrated accordingly to the absorption edge of Cu foil. Athena and Artemis codes were used to extract the data and fit the profiles. For the X-ray absorption near edge structure (XANES) part, the experimental absorption coefficients as function of energies μ(E) were processed by background subtraction and normalization procedures, and reported as "normalized absorption". For the extended X-ray absorption fine structure (EXAFS) part, the Fourier transformed (FT) data in R space were analyzed by applying first-shell approximate model for Cu-O contributions. The parameters describing the electronic properties (e.g., correction to the photoelectron energy origin, E_0) and local structure environment including CN, bond distance (R) and Debye-Waller (D.W.) factor around the absorbing atoms were

allowed to vary during the fit process. The fitted range for k space was selected to be k = 3-10 $Å^{-1}$ (k3 weighted).

Electrochemical measurements

All electrochemical CO_2RR measurements were carried out via H-type electrolytic cells with 35 mL 1 M KOH electrolyte in the cathode compartment and anode, respectively. The cathode and anode compartment were separated by a Nafion 117 membrane. The electrochemical data was collected by an electrochemical workstation (CHI760e). For the working electrode, 2 mg of the prepared catalyst was dispersed into 210 μL of a mixed solution (100 μL isopropanol, 100 μL deionized water, 10 μL 5% Nafion solution) by sonicating for about 40 minutes to form a uniform ink.100 μL of the catalyst ink was sprayed on an porous carbon paper with 1 cm^2 area resulting in a catalyst loading of 1 mg cm^{-2}. Saturated calomel electrode (SCE, saturated KCl) electrode and a Pt wire serve as the reference and counter electrodes, respectively. Linear sweep voltammetry (LSV) was performed at a scan rate of 10 mV s^{-1}. All measured potentials were calibrated to RHE using the following equation: E (relative to RHE) = E (relative to SCE) + 0.241V + 0.0591pH, and were recorded without iR compensation.

To start the experiment, the reaction system was purged with CO_2 at a flowing rate of 30 sccm for at least 30 min and the solution was stirred at 300 rpm to saturate the 1 M KOH solution. The gaseous products were quantified by gas chromatography, in which CO and other multi-carbon products were measured by flame ionization

detector (FID) and H_2 was measured by thermal conductivity detector (TCD). Highpurity Argon (99.999%) was used as the carrier gas. Liquid products were characterized by ^{1}H NMR spectra measured on a 400 MHz NMR spectrometer (Bruker Avance III 400 HD spectrometer). Before measurement, 0.5 mL of catholyte was taken out from the electrochemical cell after 60 min of CO_2 electroreduction, and then 0.1 mL D_2O (which contained DMSO as an internal standard) was added, 0.6 mL of the mixture was mixed and transferred to an NMR sample tube for quantitative analysis of the product.

The Faraday efficiency of products was calculated by the following formula:

$$\text{FE (\%)} = \frac{neF}{Q} \times 100\%$$

where e is the number of electrons transferred (for example, e = 2 for reduction of CO_2 to CO), F is Faraday constant (F=96485 C/mol), n is the mole fraction of the product, and Q is the total charge.

Operando Raman measurement

The operando Raman measurement was carried out on a Raman spectroscopy equipped (LabRAM HR Evolution, HORIBA). The measurement was performed in an electrochemical cell with a Pt wire and a saturated calomel electrode as the counter and reference electrode, respectively. For potential-resolved operando Raman spectroscopy, the collection time was 10 min.

DFT calculations

Density functional theory (DFT) calculations were performed by the Vienna Nonlinear Simulation Package (VASP) using the Projected Augmented Wave (PAW) method. The energy cutoff was set to 450 eV and the Brillouin zone was optimized as a 2×2×1 k-point grid. The convergence energy and force norms for electron energy and stress on each atom were 1×10^{-5} eV and 0.01 eV $Å^{-1}$, respectively. All calculations were performed considering spin polarization. For DOS calculations, a larger k-point grid of 3×3×1 was sampled in the Brillouin zone.

For CO_2RR, the computational hydrogen electrode model employs the Gibbs free-energy change curves to estimate the activity of the catalyst. Free energy change from initial states to final states of the reaction was calculated as follows:

$$\Delta G = \Delta E + \Delta ZPE - T\Delta S$$

where ΔE is the total energy change based on the DFT calculations, ΔZPE and ΔS are the change in the zero-point energy and the entropy, respectively. T is room temperature (298.15 K). The free energy of ($H^+ + e^-$) at standard conditions was assumed as the energy of 1/2 H_2. The entropies of the CO_2RR intermediates were calculated from the vibrational frequencies.

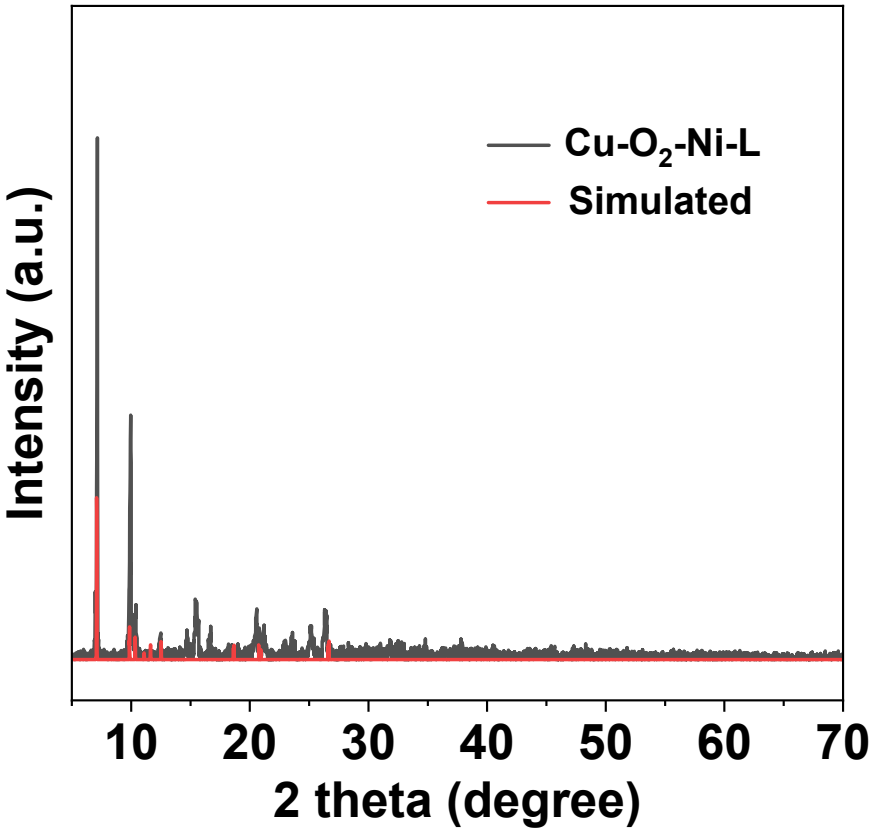

Figure S1. Simulated and experimental XRD patterns of L(Cu-O_2-Ni).

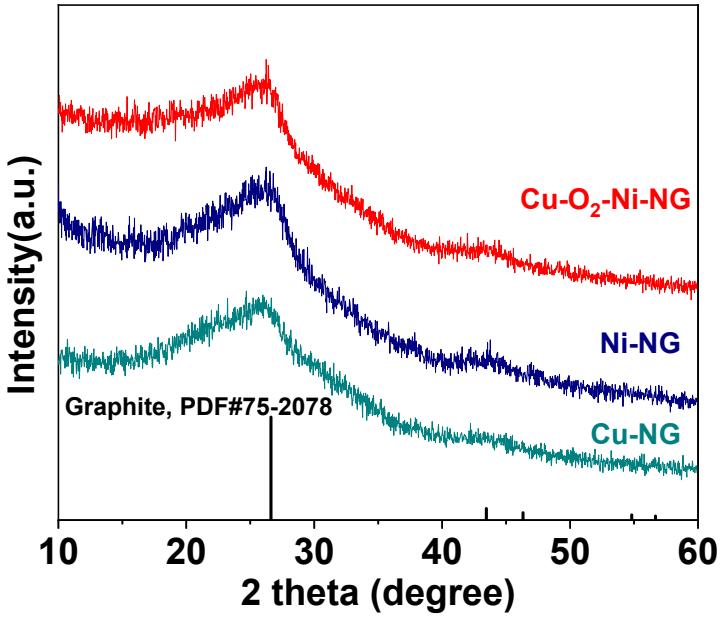

Figure S2. XRD patterns of Cu-O_2-Ni-NG, Ni-NG and Cu-NG.

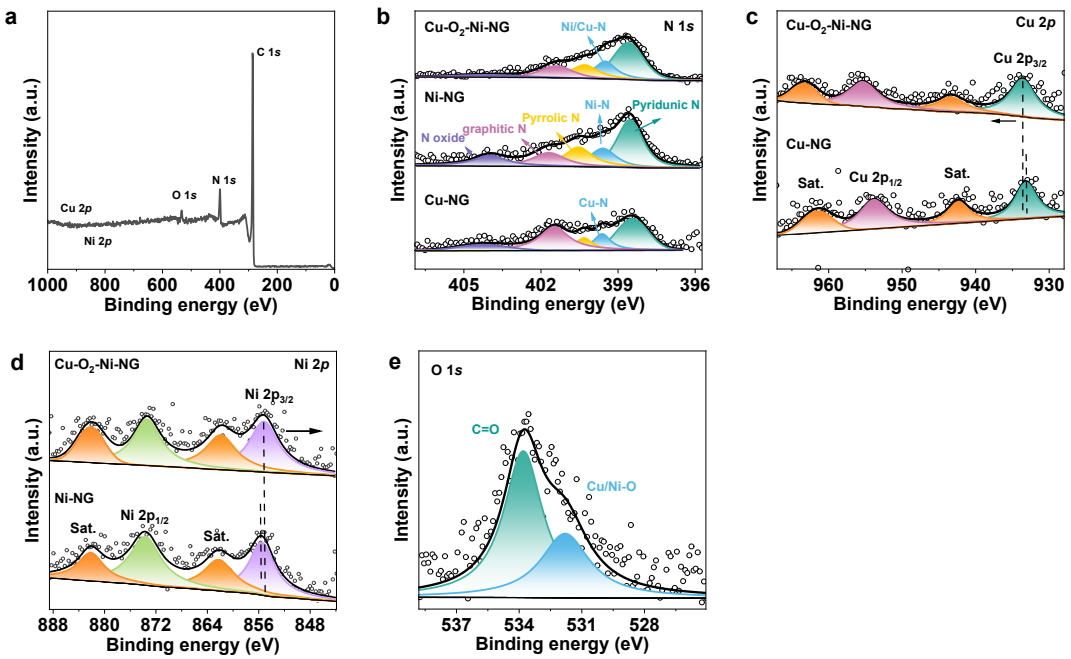

Figure S3. (a) XPS survey spectra of Cu-O_2-Ni-NG. High resolution XPS spectra for (b) N 1*s*, and (c) Cu 2*p*, (d) Ni 2*p*, (d) N 1*s* of Cu-O_2-Ni-NG, Cu-NG and Ni-NG and (e) O 1*s* of Cu-O_2-Ni-NG.

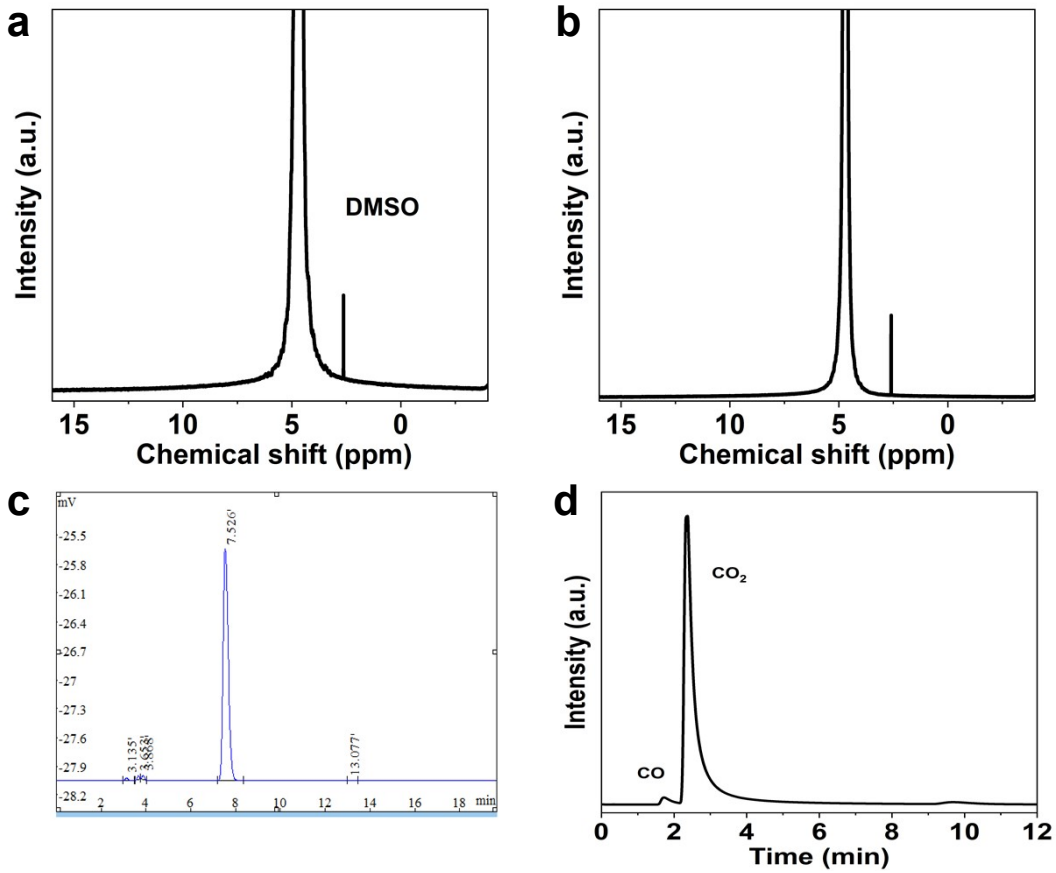

Figure S4. (a) ^{1}H NMR of simple electrolyte solution. (b) ^{1}H NMR of electrolyte solutions obtained using Cu-O_2-Ni-NG at -1.05 V vs. RHE (c) TCD plot report and (d) FID plot report obtained using Cu-O_2-Ni-NG at -1.05 V vs. RHE.

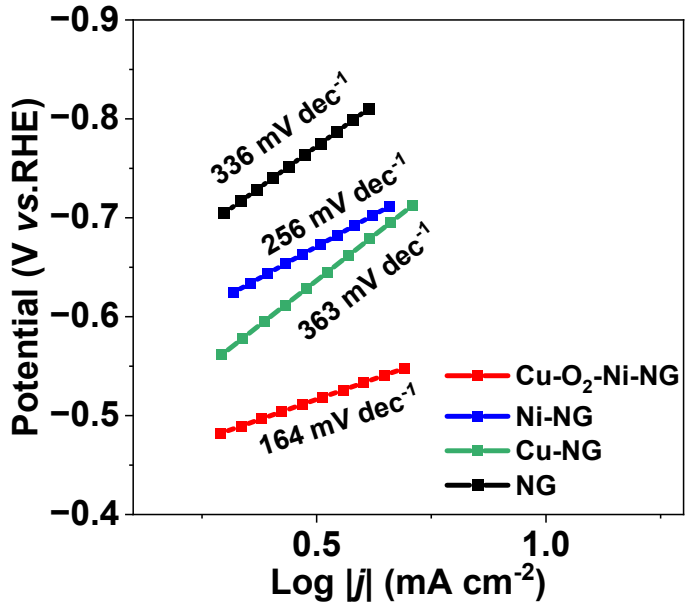

Figure S5. (a) Tafel slopes of the NG, Cu-NG, Ni-NG and Cu-O_2-Ni-NG.

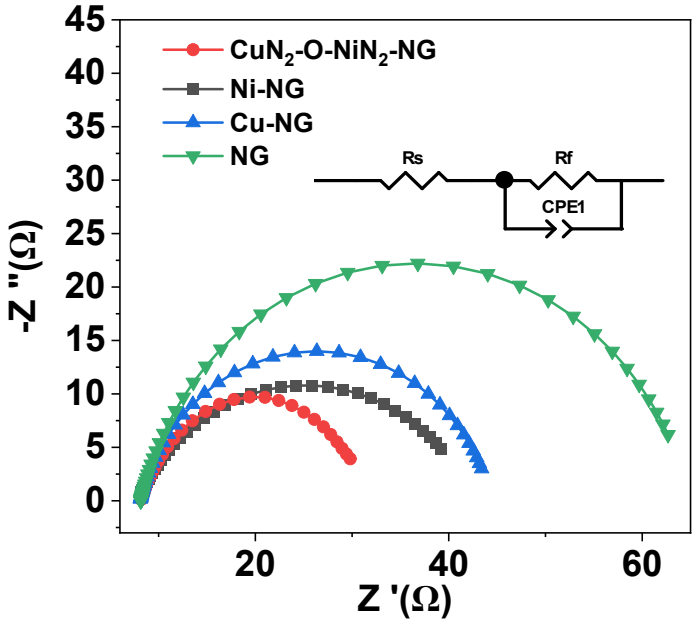

Figure S6. Electrochemical impedance spectroscopy (EIS) curves of the NG, Cu-NG, Ni-NG and Cu-O_2-Ni-NG.

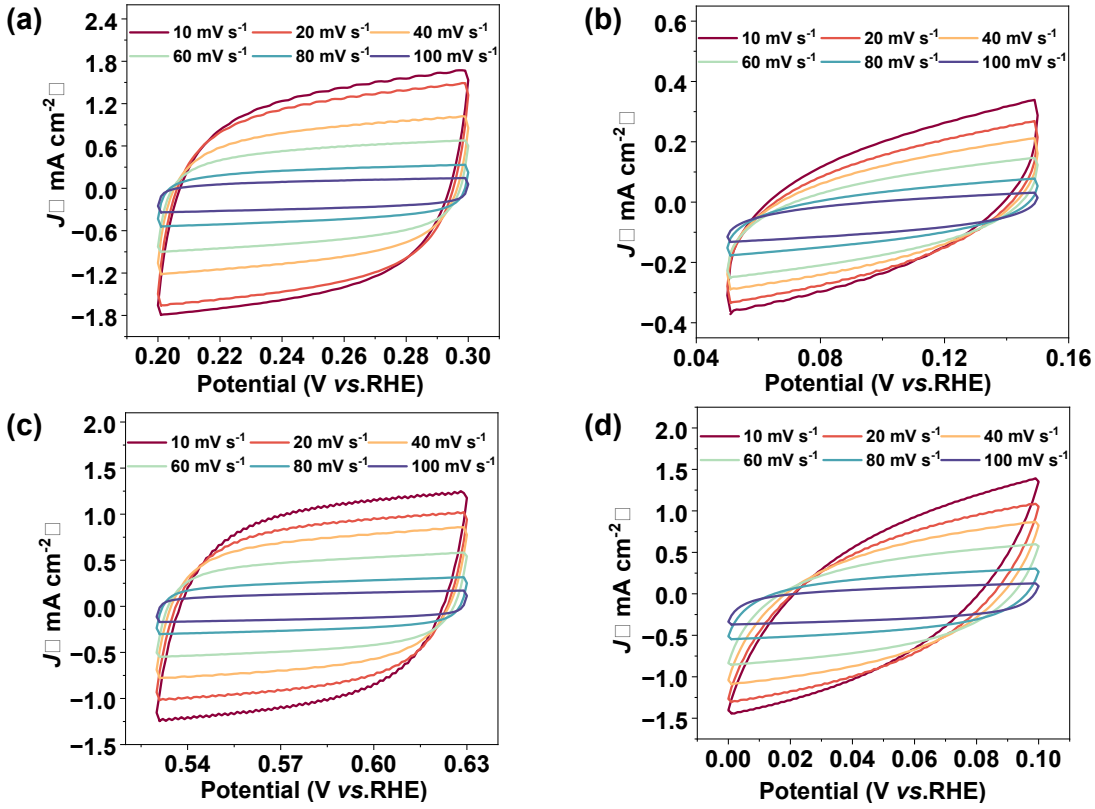

Figure S7. CV curves in 1 M KOH electrolyte at scanning rates from 10 to 100 mV s^{-1} of (a) Cu-O_2-Ni-NG, (b) Cu-NG, (c) Ni-NG, and (d) NG.

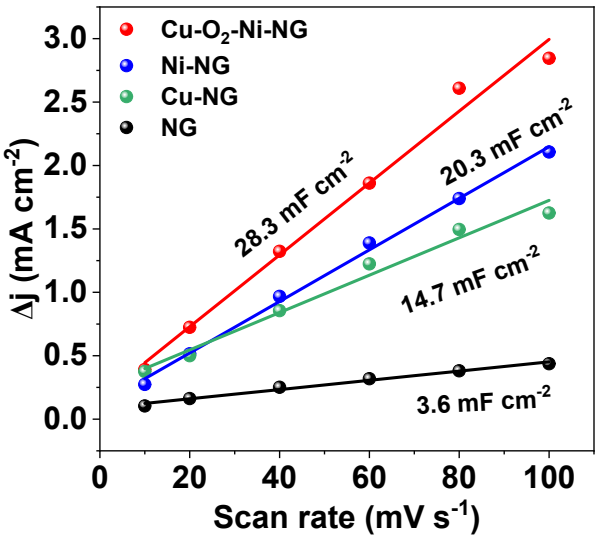

Figure S8. Double-layer charging current densities for NG, Cu-NG, Ni-NG and Cu-O_2-Ni-NG.

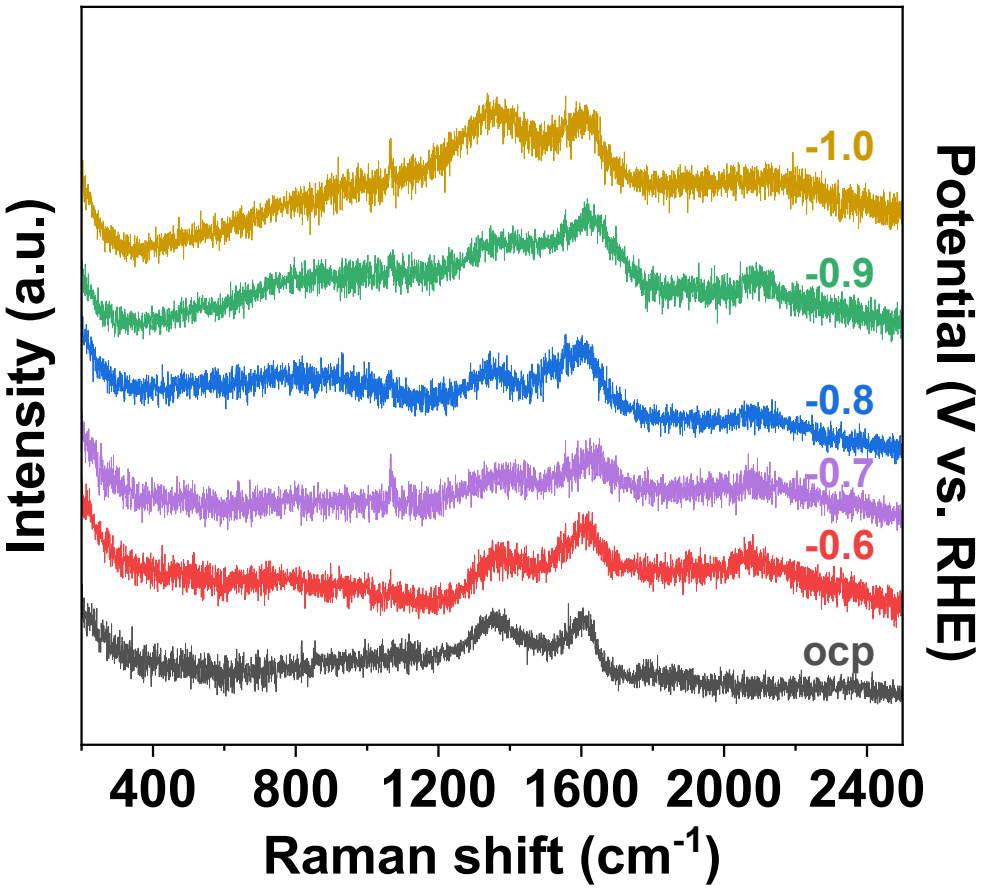

Figure S9. Operando Raman spectroscopic study on the intermediate adsorption.

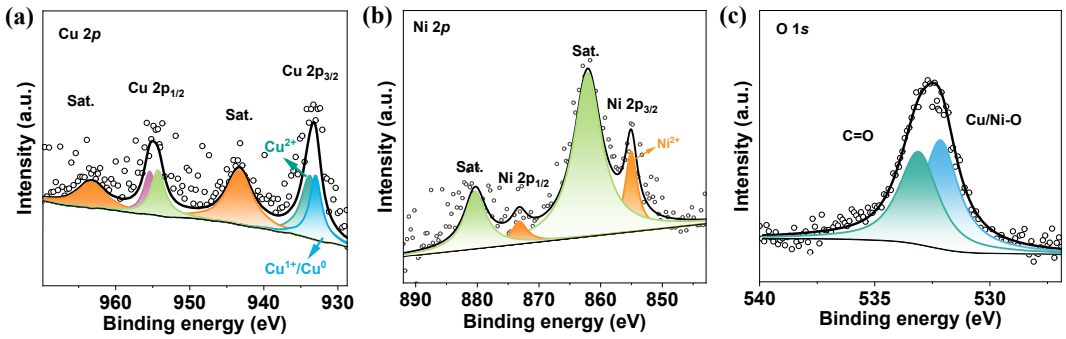

Figure S10. XPS spectra of Cu 2*p*, Ni 2*p* and O1*s* peaks for Cu-O_2-Ni-NG after testing.

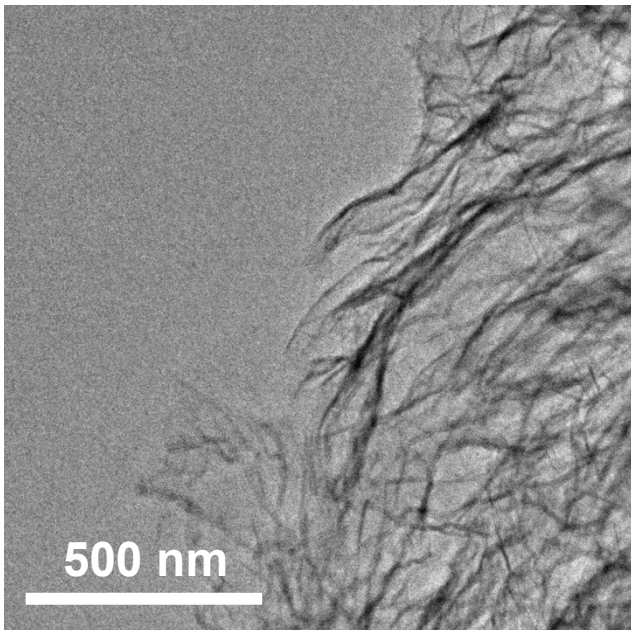

Figure S11. Post-reaction TEM images of Cu-O_2-Ni-NG.

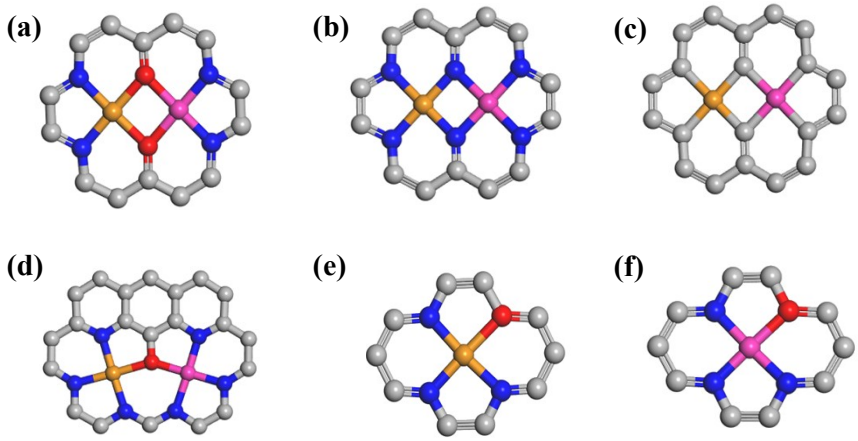

Figure S12. The stable structure of the Cu-N_2-Ni-NG, Cu-N_2-Ni-NG, CuNi-NG, Cu-O-Ni-NG, Cu-NG and Ni-NG.

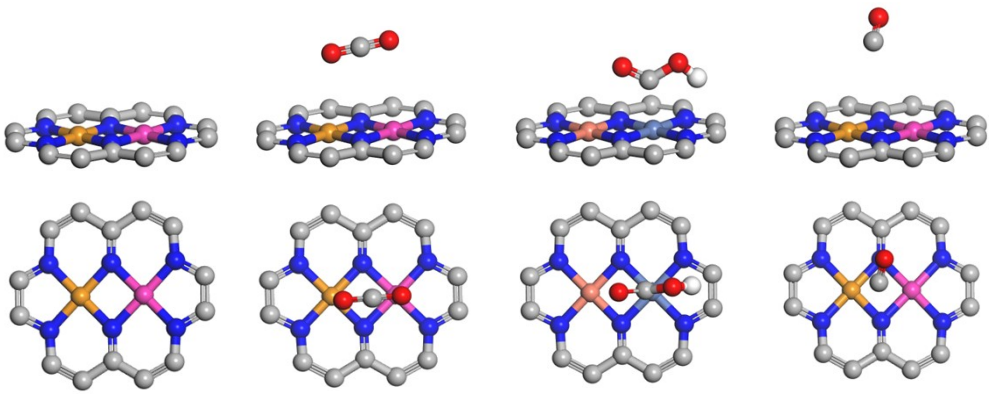

Figure S13. The stable structure of the Cu-N_2-Ni-NG model and the intermediate structure of the CO_2RR catalytic reaction.

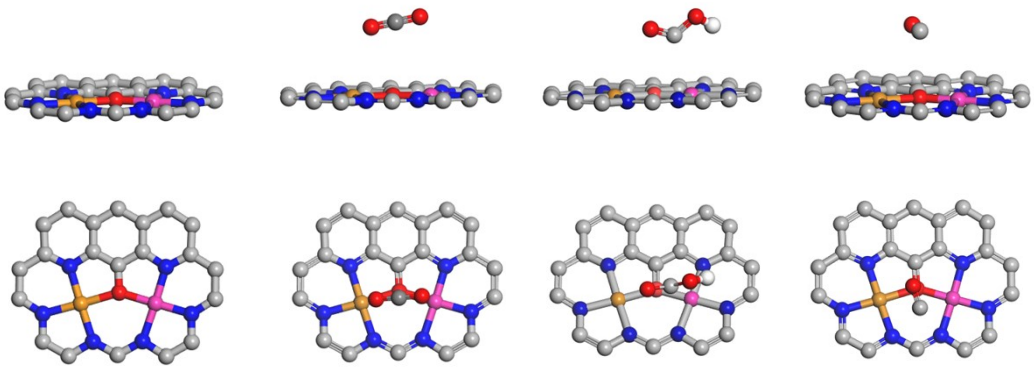

Figure S14. The stable structure of the Cu-O-Ni-NG model and the intermediate structure of the CO_2RR catalytic reaction.

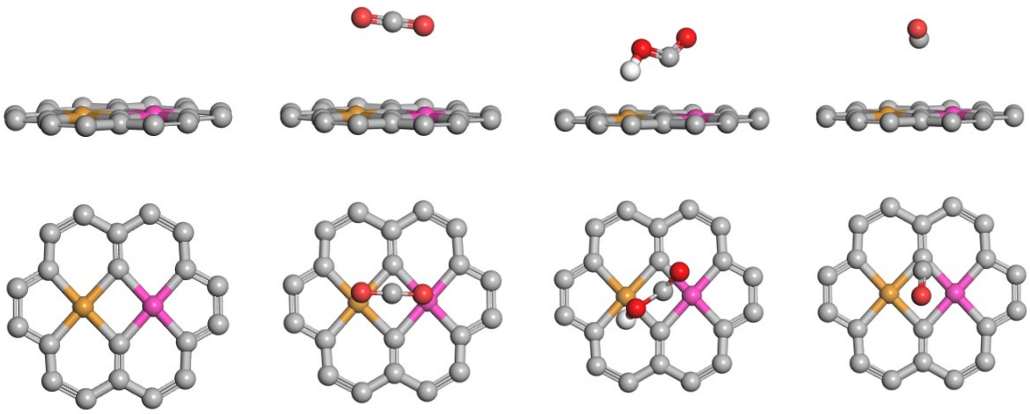

Figure S15. The stable structure of the CuNi-NG model and the intermediate structure of the CO_2RR catalytic reaction.

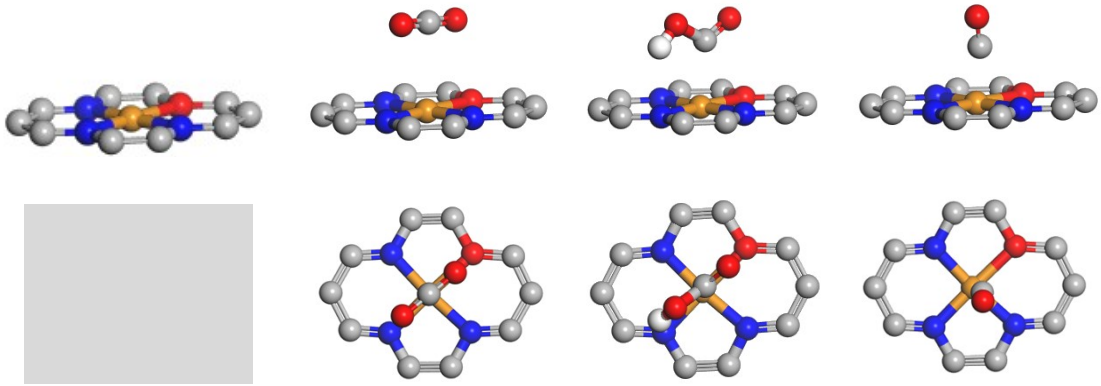

Figure S16. The stable structure of the Cu-NG model and the intermediate structure of the CO_2RR catalytic reaction.

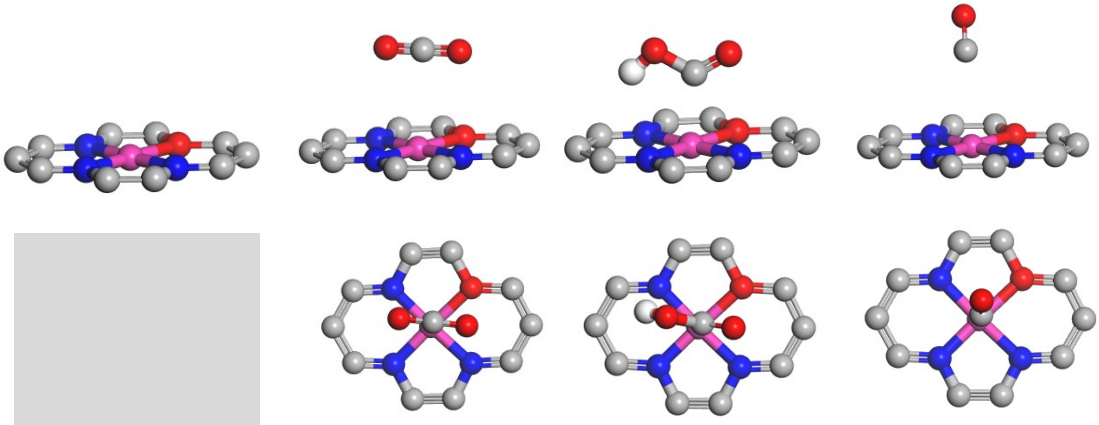

Figure S17. The stable structure of the Ni-NG model and the intermediate structure of the CO_2RR catalytic reaction.

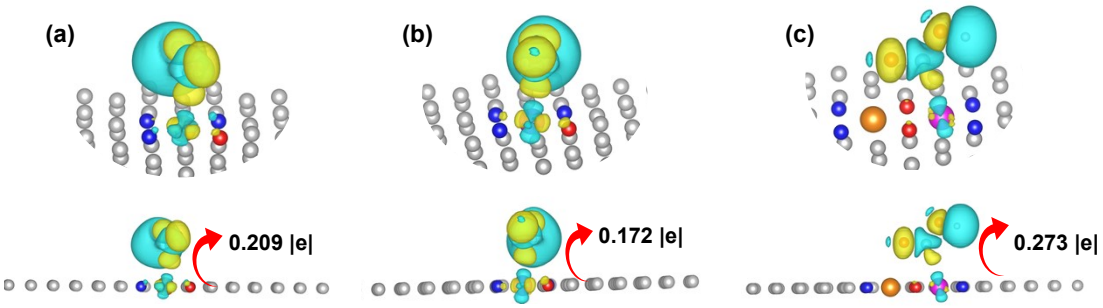

Figure S18. Charge density differences for *COOH adsorption configurations on (a) Cu-NG, (b) Ni-NG and (c) Cu-O_2-Ni-NG

Table S1. Curve fit parameters of Cu and Ni K-edge EXAFS for Cu-O_2-Ni-NG

Sample	Path	N	R (Å)	σ^2 (10^{-3}Å^2)	ΔE_0 (eV)	R factor
Cu-O_2-Ni-NG-Cu	Cu-N/O	3.20±0.16	1.85±0.025	0.008	7.61	0.007
	Cu-O-Ni	1.28±0.09	2.59±0.028	0.001		
Cu-O_2-Ni-NG-Ni	Ni-N/O	3.11±0.18	1.95±0.045	0.005	8.75	0.003
	Ni-O-Cu	1.42±0.12	2.67±0.028	0.009		
Cu-O_2-Ni-L-Cu	Cu-N/O	3.38±0.20	1.83±0.008	0.006	1.39	0.006
	Cu-O-Ni	1.44±0.04	2.58±0.009			
Cu-O_2-Ni-L-Ni	Ni-N/O	3.26±0.25	1.90±0.003	0.008	1.86	0.005
	Ni-O-Cu	1.34±0.21	2.62±0.005			
Cu-NG	Cu-N	2.78±0.31	1.95±0.016	0.006	2.67	0.008
Ni-NG	Ni-N	3.06±0.15	1.86±0.02	0.009	3.14	0.008

Table S2. Faradaic efficiencies of CO and H_2 for Cu-O_2-Ni-NG at different applied potentials

Potential (V vs. RHE)	FE_{CO} (%)	FE_{H2} (%)	Total FE (%)
-0.60	90.4	6.7	97.1
-0.75	92.1	8.9	101
-0.90	93.5	5.6	99.1
-1.05	95.2	4.1	99.3
-1.20	90	5.1	95.1

Table S3. Summary of TOF calculation parameters and values for Cu-O_2-Ni-NG, Cu-NG, and Ni-NG at -1.05 V vs. RHE

Catalyst	Cu-O_2-Ni-NG	Cu-NG	Ni-NG
J_{total} (mA cm^{-2})	62.12	21.31	25.30
FE_{CO} (%)	95.2	24.28	62.7
J_{CO} (mA cm^{-2})	59.14	5.17	15.86
Metal loading (mg cm^{-2})	2	2	2
Metal content (wt%)	Cu: 0.73, Ni: 0.84	Cu: 0.78	Ni: 1.02
N_{metal} (mol)	$5.16*10^{-7}$	$2.46*10^{-7}$	$3.48*10^{-7}$
TOF (s^{-1})	0.59	0.11	0.24

Table S4. Comparison of CO_2RR performance between oxygen bridged Cu-O_2-Ni-NG and nitrogen bridged Cu-N_2-Ni-NG

Catalyst	E (V vs. RHE)	FE_{CO} (%)	J_{CO} (mA cm^{-2})	Electrolyte
Cu-O_2-Ni-NG	-1.05	95.2	-59.1	1 M KOH
Cu-N_2-Ni-NG	-0.9	86.3	-39.2	1 M KOH

Table S5. CO_2RR performance on various SACs and DACs at 1.0 V vs. RHE

Catalyst	FE_{CO} (%)	Current density (CO)(mA cm^{-2})	Electrolyte	Reactor type	η (mV)	Ref.
Cu-O_2-Ni-NG	95.2	-56.42	1 M KOH	H-cell	316	This work
Cu-NG	62.7	5.01	1 M KOH	H-cell	316	This work
Ni-NG	28.0	15.26	1 M KOH	H-cell	316	This work
Ni-N-HCNs	95.0	≈ 19	0.5 M $KHCO_3$	H-cell	453	[1]
Cu/Ni-N_2C_2	96.0	≈ 44	0.5 M $KHCO_3$	H-cell	453	[2]
Ni-NPs	92.6	≈ 43	0.5 M $KHCO_3$	H-cell	453	[3]
Zn_1Mn_1-SNC	92.8	≈ 42(-0.9v)	0.1 $KHCO_3$	H-cell	353	[4]
ZnN_4/C	95.0	≈ 10	0.5 M $KHCO_3$	H-cell	453	[5]
Mn-N/C	92.0	≈ 29	0.5 M $KHCO_3$	H-cell	453	[6]
Co-N/C	74.0	≈ 19	0.5 M $KHCO_3$	H-cell	453	[6]

Note: All data were obtained in H-type cells. Our catalyst was tested in 1 M KOH, while most reference catalysts were tested in 0.5 M $KHCO_3$. The higher ionic conductivity and alkaline condition of 1 M KOH contribute to enhanced current densities, yet the comparison highlights the superior intrinsic activity of the oxygen-bridged Cu-O-Ni sites.

Table S6. Curve fit parameters of Cu and Ni K-edge EXAFS after the reaction of Cu-O_2-Ni-NG.

Sample	Path	N	R (Å)	σ^2 ($10^{-3}Å^2$)	ΔE_0 (eV)	R factor
Cu-O_2-Ni-NG-Cu	Cu-N/O	3.25±0.09	1.88±0.019	0.008	10.15	0.005
	Cu-O-Ni	1.39±0.025	2.63±0.028	0.003		
Cu-O_2-Ni-NG-Ni	Ni-N/O	3.11±0.18	1.95±0.045	0.005	9.75	0.006
	Ni-O-Cu	1.44±0.26	2.75±0.017	0.03		

Table S7. The HER reaction free energy of catalysts Cu-NG, Ni-NG, CuNi-NG, Cu-N_2-Ni-NG, Cu-O-Ni-NG and Cu-O_2-Ni-NG

Catalyst	Cu-NG	Ni-NG	CuNi-NG	Cu-N_2-Ni-NG	Cu-O-Ni-NG	Cu-O_2-Ni-NG
ΔG	-0.49	-0.31	0.73	0.16	0.83	0.91

References

1. Z. Liu, L. Cao, M. Wang, Y. Zhao, M. Hou and Z. Shao, *J. Mater. Chem. A*, 2024, **12**, 8331-8339.
2. Y. Zhuang, K. Wei, Z. Li, H. Gong, J. Deng, H. Yuan, H. Lian, H. Zheng, H. Zhao, X. Zhang and J. Liu, *J. Energy Chem.*, 2025, **103**, 333-343.
3. R. Boppella, Y. Kim, K. A. Joshi Reddy, I. Song, Y. Eom, E. Sim and T. K. Kim, *Appl. Catal. B Environ. Energy*, 2024, **345**, 123699.
4. J. Pei, L. Yang, J. Lin, Z. Zhang, Z. Sun, D. Wang and W. Chen, *Angew. Chem. Int. Ed. Engl.*, 2024, **63**, e202316123.
5. F. Yang, P. Song, X. Liu, B. Mei, W. Xing, Z. Jiang, L. Gu and W. Xu, *Angew.*

Chem. Int. Ed., 2018, **57**, 12303-12307.

6. M. Xie, J. Wang, X.-L. Du, N. Gao, T. Liu, Z. Li, G. Xiao, T. Li and J.-Q. Wang, *RSC Adv.*, 2022, **12**, 32518-32525.